Computation of engine noise propagation and scattering off an aircraft

D. Stanescu*, J. Xu*, M.Y. Hussaini* and F. Farassat†
*School of Computational Science and Information Technology, Florida State University, Tallahassee, Florida 32306-4120
† NASA Langley Research Center, Hampton, Virginia 23681-0001

ABSTRACT

The purpose of this paper is to demonstrate the feasibility of computing the fan inlet noise field around a real twin-engine aircraft, which includes the radiation of the main spinning modes from the engine as well as the reflection and scattering by the fuselage and the wing. This first-cut large-scale computation is based on time domain and frequency domain approaches that employ spectral element methods for spatial discretization. The numerical algorithms are designed to exploit high-performance computers such as the IBM SP4. Although the simulations could not match the exact conditions of the only available experimental data set, they are able to predict the trends of the measured noise field fairly well.

1. INTRODUCTION

The fan inlet and exhaust noise are among the major components of the noise signature of an aircraft at take-off and landing. The noise radiated to the far field by the engine of an aircraft is largely influenced both by the flow around the wing and fuselage and by the scattering from various other aircraft surfaces. In principle, it is possible to reduce the aircraft noise footprint by taking advantage of engine and wing location and manipulating the flow around the aircraft. Experimental investigations of these phenomena are difficult to perform and extremely expensive. Numerical simulations offer a relatively inexpensive alternative, and such simulations are becoming increasingly attractive due to the recent advances in the performance of both computers and computational methods. To date, most measurements and modeling of engine noise are confined to isolated engines [8, 6, 7]. Recently, Stanescu, Hussaini, and Farassat [19] have computed the engine noise propagation and scattering for a generic aircraft configuration by numerically solving the Euler equations with a discontinuous Galerkin spectral element method. The recent popularity of such methods in aerodynamic applications stems from the fact that they require relatively few points per wavelength,

they have low dispersion and dissipation errors [5, 18, 10], they have geometric flexibility [11, 13], and they are compact, robust and inherently parallelizable [19, 12]. In a more recent work [20], the authors developed a spectral element method for the solution of the acoustic potential equation, in the frequency domain, in the presence of a non-uniform mean flow field. The two approaches are complementary prediction tools that can be used for computing tonal sound propagation and scattering in the near field of the engine.

The aim of this paper is to show that large-scale modeling (in terms of scale, frequency and spinning mode order) of tone noise propagation from an actual nacelle and scattering by a realistic aircraft configuration is now feasible at actual operating conditions. To this end, we consider the problem of fan inlet noise of a two-engine business jet aircraft, and construct high-performance algorithms based on the aforementioned numerical methodology. After a brief discussion of the time-domain and frequency-domain spectral element approaches in the next section, we present the computed results obtained for several flight regimes versus the available experimental data collected on the wing. To conduct the numerical experiments, the modal composition of the acoustic signal inside the duct in terms of spinning modes is used to specify the source. Rotating rake measurements of these modes have been performed on an isolated engine by Sutliff, Konno and Heidelberg [21]. However, for the maximum power condition at which the experimental data were collected, modal data is not available. In lack of an exact definition, the source is specified using modal data at a somewhat lower power setting for which the rotor tip speed is also supersonic. Even in this case, due to interference with the rake wake, the data for the rotor-locked mode, expected to be the dominant mode at large power settings, is contaminated in the measurements presented by Sutliff [21]. Under these circumstances, in order to gain insight into the propagation characteristics of the different spinning modes, several source definitions have been considered. These include individual spinning modes as well as a combination of four spinning modes with amplitude levels in agreement with the data for 88 percent maximum speed. Although the flight conditions could not be duplicated exactly in the present computations, results show that the noise signatures computed in this way match well the trend of the experimental data.

2. PROBLEM FORMULATION AND SOLUTION TECHNIQUE

2.1. Computational model

We assume that the engine noise source is known and consider noise propagation and scattering in the left half space implicitly assuming symmetry of the problem about the $y = 0$ plane which is chosen to bisect the aircraft along the fuselage. For computational purpose the half space is truncated into a bounded computational domain comprised of a physical domain with a damping layer surrounding it. The latter is used to ensure that the physical domain remains uncontaminated by reflections. The surface that separates the computational domain from the surrounding medium is denoted by Γ_∞, and the engine tone noise source is specified as a combination of spinning modes on a circular disc surface Γ_f appropriately situated inside the nacelle. The governing equations are solved in non-dimensional form. The reference quantities for non-dimensionalization are: ρ_∞ for the density, c_∞ for the velocity components, $\rho_\infty c_\infty^2$ for the pressure, the radius R of the noise-source disc for distance, and $\frac{R}{c_\infty}$ for time.

The physical domain is defined in the non-dimensional Cartesian coordinates as $25.0 \leq x \leq 36.5$, $-8.5 \leq y \leq 0.0$ and $1.3 \leq z \leq 8.2$, and the full domain of computation (including the damping layers) is defined as $21.4 \leq x \leq 40.0$, $-12.0 \leq y \leq 0.0$ and $-1.8 \leq z \leq 11.2$. The computational domain with the embedded aircraft is depicted in Fig. 1. As the propagation distance is relatively small, viscous effects are neglected, and the problem is assumed to be governed by inviscid compressible flow equations.

The computational domain is covered by a grid of non-overlapping hexahedral elements that can have curved boundaries. The ICEMCFD Hexa commercial package is used to generate the unstructured hexahedral grid around the aircraft configuration. Once an unstructured grid of hexahedra is generated, an attractive new feature of this package allows for the generation of points along each of the edges of the hexahedral mesh, which can be either a Legendre-Lobatto or a Chebyshev-Lobatto distribution for a specified polynomial of degree N. Fig. 2 shows the hexahedral representation of the underlying geometry with Gauss-Legendre point distribution, for sixth order ($N = 6$) elements. All the necessary point coordinates can then be computed by interpolation based on the spectral interpolants along the edges (to obtain coordinates at the Gauss points from the Lobatto points on the edges) followed by three-dimensional transfinite interpolation [3] on the faces and inside the elements.

2.2. Time domain formulation

For the time domain formulation, the governing equations are the Euler equations in Cartesian conservation form,

$$\frac{\partial \tilde{Q}}{\partial t} + \sum_{d=1}^{3} \frac{\partial \tilde{F}_d}{\partial x_d} = 0. \tag{1}$$

where the state vector $\tilde{Q}$ and the flux vector $\tilde{F}_d$ are given by

$$\tilde{Q} = \begin{pmatrix} \rho \\ \rho v_1 \\ \rho v_2 \\ \rho v_3 \\ \rho E \end{pmatrix}, \ \tilde{F}_d = \begin{pmatrix} \rho v_d \\ \rho v_1 v_d + p\delta_{1d} \\ \rho v_2 v_d + p\delta_{2d} \\ \rho v_3 v_d + p\delta_{3d} \\ (\rho E + p) v_d \end{pmatrix}, \tag{2}$$

with ρ the fluid density, E the specific internal energy, p the pressure, and v_d $(d = 1, 2, 3)$ the velocity components.

Each element of the grid is mapped onto the master element $\Omega_M = [-1, 1]^3$ with an isoparametric transfinite interpolation transformation [3] for the expediency of representing the solution in each element by spectral basis functions defined on the interval $[-1, 1]$. Under the mapping, Eq. (1) becomes

$$\frac{\partial Q}{\partial t} + \sum_{d=1}^{3} \frac{\partial F_d}{\partial \xi_d} = 0, \tag{3}$$

where Q and F are the transformed components of the state and flux vectors

$$Q = J\tilde{Q}, \quad F_d = J \sum_{m=1}^{3} \frac{\partial \xi_d}{\partial x_m} \tilde{F}_m, \tag{4}$$

and J is the Jacobian of the transformation,

$$J = \det \left(\frac{\partial(x_1, \ldots, x_3)}{\partial(\xi_1, \ldots, \xi_3)} \right). \tag{5}$$

The computational space coordinates are denoted by either (ξ_1, ξ_2, ξ_3) or (ξ, η, ζ) hereafter for convenience.

Let the space of polynomials of degree N in $\xi \in [-1, 1]$ be denoted by $P_N(\xi)$. A basis for this space can be constructed using the Lagrange interpolating polynomials $h_j, j = 0, 1, \ldots, N$, through the $N + 1$ Gauss-Legendre [2] quadrature nodes ξ_i, $i = 0, 1, \ldots, N$. These polynomials are

given explicitly by

$$h_j(\xi) = \prod_{i=0, i\neq j}^{N} \frac{(\xi - \xi_i)}{(\xi_j - \xi_i)}, \quad h_j(\xi_i) = \delta_{ij}. \tag{6}$$

The three-dimensional solution Q is searched in the trial space obtained as a tensor product of one-dimensional polynomials of degree N for each coordinate direction, i.e. in $P_N^3 = P_N(\xi) \times P_N(\eta) \times P_N(\zeta)$. Hence the solution takes the form

$$Q(t, \xi, \eta, \zeta) = \sum_{i=0}^{N}\sum_{j=0}^{N}\sum_{k=0}^{N} Q_{ijk}(t) h_i(\xi) h_j(\eta) h_k(\zeta) \tag{7}$$

where $Q_{ijk}(t)$ denote point-wise values of Q at time t. This form of the solution allows for the efficient evaluation through Gauss quadrature of the volume integrals inherent in the formulation. A discontinuous Galerkin approximation [19] is obtained by requiring

$$(Q_t, \phi_{ijk}) + (\nabla_\xi \cdot F, \phi_{ijk}) = 0 \tag{8}$$

to be satisfied for all triplets $(i, j, k) \in \{0, 1, \ldots, N\}^3$. In the above equation, $(\cdot, \cdot)$ represents the usual L^2 inner product, and $\phi_{ijk} = h_i(\xi) h_j(\eta) h_k(\zeta)$ are the basis functions of P_N^3.

Using the divergence theorem, equation (8) is recast in the weak form

$$(Q_t, \phi_{ijk}) + \int_{\partial\Omega_M} \phi_{ijk} F \cdot n dS = (F, \nabla_\xi \phi_{ijk}). \tag{9}$$

The volume integrals are now evaluated through Gauss quadrature,

$$\int_{-1}^{1} f(\xi) d\xi = \sum_{m=0}^{N} f(\xi_m) w_m, \ \forall f \in P_{2N+1} \tag{10}$$

w_m being the Gauss weights. This integration is exact for elements with straight edges, in which case J is a polynomial of degree one, and the first integrand in equation (9) is a polynomial of degree $2N + 1$. In the case of elements with curved boundaries, which in our discretization appear only adjacent to the boundaries, a discretization error decreasing exponentially with the order N appears due to the quadrature (10).

Expanding the boundary integral and performing some algebraic manipulation, one finds the final discrete form of the equations governing each

variable at the Legendre-Gauss points,

$$\frac{dQ_{ijk}}{dt} = -\left[D^{\xi} + D^{\eta} + D^{\zeta}\right] F, \tag{11}$$

where the right-hand side is a sum of discrete differential operators acting on the flux values of an element, which include values on the element faces. Here, the differential operator $D^{\xi}F$, for example, is defined as

$$D^{\xi}F = \frac{1}{w_i}\left[F_1^*(1,\eta_j,\zeta_k)h_i(1) - F_1^*(-1,\eta_j,\zeta_k)h_i(-1) - d^{\xi}F\right], \tag{12}$$

where F^* denotes a common face flux, which can be computed directly from the values of the state vector as explained below. $D^{\eta}F$ and $D^{\zeta}F$ follow by obvious permutations.

As the solution is approximated by a polynomial that passes through interpolation nodes distributed within the elements, a mismatch ensues when the interpolants are evaluated at element interfaces [16]. This mismatch in the solution at element boundaries is resolved by solving a Riemann problem for the interface flux, similar to finite volume methods [14, 4]. This leads to a semi-discrete form of Euler equations, which represents an ordinary differential equation (ODE) system. The resulting ODE system is integrated in time using a low-storage Runge-Kutta scheme optimized for wave propagation [15]. Acoustic perturbations are obtained at each time step by subtracting the mean flow from the total flow variables, and the RMS pressure is obtained by integrating in time the acoustic pressure. This integration is only performed after sufficient time is allowed for the acoustic signal from the source to propagate through the computational domain and establish a periodic acoustic field.

2.3. Frequency domain formulation

The equation governing the acoustic field is in this case obtained by considering the flow irrotational, so that the continuity equation becomes

$$\frac{\partial \rho}{\partial t} + \nabla \cdot (\rho \nabla \Phi) = 0 \tag{13}$$

where ρ is the fluid density, and Φ is the total velocity potential, $\mathbf{V} = \nabla\Phi$. Under the isentropic assumption, the momentum equation is reduced to an

algebraic relation relating the density to the velocity potential as

$$\rho = \left[1 - (\gamma - 1)\left(\frac{\partial \Phi}{\partial t} + \frac{(\nabla \Phi)^2 - M_\infty^2}{2}\right)\right]^{\frac{1}{\gamma - 1}} \tag{14}$$

where M_∞ is the far field Mach number and γ the specific heats ratio. Consider the unsteady flow field resulting from the superposition of small acoustic perturbations, denoted by a prime, on a steady, irrotational, mean flow denoted by an overbar: $\rho = \bar{\rho} + \rho'$ and $\Phi = \bar{\Phi} + \Phi'$. The partial differential equation governing the acoustic perturbations is

$$\frac{\partial \rho'}{\partial t} + \nabla \cdot (\bar{\rho} \nabla \Phi' + \rho' \nabla \bar{\Phi}) = 0 \tag{15}$$

with the following relation relating the acoustic density to the acoustic velocity potential, obtained by linearization of equation (14):

$$\rho' = -\frac{\bar{\rho}}{\bar{c}^2}\left[\frac{\partial \Phi'}{\partial t} + \nabla \bar{\Phi} \cdot \nabla \Phi'\right]. \tag{16}$$

For a frequency domain approach, the acoustic potential is considered to be of the form $\Phi' = \phi(x, y, z)\exp(i\omega t)$. In view of a weak formulation, the governing equation (15) is multiplied by a test function $\Psi' = \psi(x, y, z)\exp(-i\omega t)$ and integrated using the divergence theorem to yield

$$\begin{aligned} &\int_\Omega \psi \frac{\partial \rho'}{\partial t} r d\Omega - \int_\Omega \nabla \psi \cdot (\bar{\rho} \nabla \phi + \rho' \nabla \bar{\phi}) r d\Omega + \\ &\int_{\Gamma_f} \psi (\bar{\rho} \nabla \phi + \rho' \nabla \bar{\phi}) \cdot \mathbf{n} r ds = 0 \end{aligned} \tag{17}$$

Account has been taken in equation (17) of the fact that the normal components of the mean flow velocity and the acoustic perturbation velocity are both zero on the aircraft surface, so that the surface integrand cancels there. Furthermore, this integrand is set to zero artificially on the Γ_∞ surface, which does not sensibly affect the computed solution since the acoustic field is strongly damped in the absorbing layer.

Let $\mathbf{Z}$ denote the complex vector space of functions that are continuous on Ω, whose restrictions to an element are polynomials of degree at most N in each variable, where N is a specified integer. Furthermore, let $\mathbf{Z}_D \subset \mathbf{Z}$ be the subset of functions that satisfy the specified Dirichlet boundary condition

on the source surface Γ_f, and $\mathbf{Z}_{\Gamma_f} \subset \mathbf{Z}$ the subset of functions with zero restriction on Γ_f. Substituting the expression for density from the linearized momentum equation, the following variational problem is obtained: find $\phi \in \mathbf{Z}_D$ such that

$$\begin{aligned}
&\int_\Omega \frac{\bar{\rho}}{\bar{c}^2} \Big[\omega^2 \phi\psi + i\omega\bar{u}\left(\phi\psi_x - \psi\phi_x\right) + \\
&i\omega\bar{v}\left(\phi\psi_y - \psi\phi_y\right) + i\omega\bar{w}\left(\phi\psi_z - \psi\phi_z\right) + \\
&\left(\bar{u}^2 - \bar{c}^2\right)\phi_x\psi_x + \left(\bar{v}^2 - \bar{c}^2\right)\phi_y\psi_y + \\
&\left(\bar{w}^2 - \bar{c}^2\right)\phi_z\psi_z + \bar{u}\bar{v}\left(\phi_x\psi_y + \phi_y\psi_x\right) + \\
&\bar{u}\bar{w}\left(\phi_x\psi_z + \phi_z\psi_x\right) + \bar{v}\bar{w}\left(\phi_y\psi_z + \phi_z\psi_y\right) - \\
&\psi\sigma\left(i\omega\phi + \bar{u}\phi_x + \bar{v}\phi_y + \bar{w}\phi_z\right)\Big]\, d\Omega = 0
\end{aligned} \tag{18}$$

holds for any $\psi \in \mathbf{Z}_{\Gamma_f}$.

This equation is discretized by a Chebyshev spectral element method [9, 17] using a basis consisting of tensor products of the Lagrange interpolants through the Chebyshev-Gauss-Lobatto points in the element. Upon evaluating the integrals, a complex linear algebra problem of the form $A\{\phi\} = \{b\}$ results, where $\{\phi\}$ represents the vector of point values of the acoustic potential ϕ.

2.3.1. High-performance Implementation

The solution of this system is obtained by a Schur complement domain-decomposition method. It is implemented using the Message Passing Interface (MPI) standard. The matrix is stored in sparse mode (i.e. only the non-zeroes are stored), with each processor only storing a number of lines in the matrix. Let P denote the total number of processors. The computational domain Ω is subdivided in as many partitions, and the unknowns situated on the surface $\mathcal{B}$ which separates the partitions are numbered last in the system and denoted by ϕ_B. For every processor p, there will be a number of unknown ϕ values located on $\mathcal{B}$. The vector of unknowns is partitioned as

$$\{\phi\} = \left\{\phi_I^1 \ldots \phi_I^P \ \phi_B\right\} \tag{19}$$

where ϕ_I^p denotes all the unknowns in sub-partition p not located on $\mathcal{B}$. The right-hand side vector $\{b\}$ is partitioned accordingly. The matrix A can then

be written in the form

$$A = \begin{pmatrix} A^1_{II} & 0 & \dots & A^1_{IB} \\ 0 & A^2_{II} & \dots & A^2_{IB} \\ . & . & . & . \\ A^1_{BI} & A^2_{BI} & \dots & A_{BB} \end{pmatrix} \tag{20}$$

and straightforward elimination of the terms below the main diagonal leads to

$$\begin{pmatrix} A^1_{II} & 0 & \dots & A^1_{IB} \\ 0 & A^2_{II} & \dots & A^2_{IB} \\ . & . & . & . \\ 0 & 0 & \dots & S \end{pmatrix} \begin{Bmatrix} \phi^1_I \\ \phi^2_I \\ . \\ \phi_B \end{Bmatrix} = \begin{Bmatrix} b^1_I \\ b^2_I \\ . \\ b_S \end{Bmatrix} \tag{21}$$

where $b_S = b_B - \sum_p A^p_{BI}(A^p_{II})^{-1} b^p_I$. The problem has thus been reduced to solving a reduced system with matrix $S = A_{BB} - \sum_p A^p_{BI}(A^p_{II})^{-1} A^p_{IB}$ for the points on $\mathcal{B}$ only, followed by a solution on each domain of the interior problem. The matrix S is much denser than the original matrix A, and its direct computation and storage is not efficient or even possible in most cases. However, for an iterative method, only the action of S on a vector is needed, and once the sparse, distributed, matrix A_{BB} is formed, this action can be computed by matrix-vector multiplications and solutions with A^p_{II}, which are local operations on processor p and do not require communications, followed by accumulation in the global vector ϕ_B. All computations can be conveniently implemented by use of the high level primitives in the PETSc [1] software. A preconditioner based on the readily available diagonal part of A_{BB} is used for the iterative solution of S.

2.4. Boundary conditions

A zero normal velocity boundary condition is imposed on the symmetry surface $y = 0$ (this supposes that the engines are symmetrically placed on either side of the fuselage and rotate in opposite sense) as well as on the fuselage, nacelle and wing surfaces. The boundary conditions on the other sides of the computational domain that make up Γ_∞ are treated by a damping layer method [16]. The physical domain is surrounded by an absorbing layer wherein the equations are modified to include a damping term which insures an exponential decay of the perturbation as it travels through the layer. The modified equations can be written in the generic

form:

$$\frac{\partial \tilde{Q}}{\partial t} + \nabla \cdot \tilde{F} = -\sigma(\mathbf{x})\tilde{Q} \tag{22}$$

where for the frequency-domain formulation $\tilde{Q} = \rho'$ together with the corresponding definition of $\tilde{F}$. The damping parameter σ is allowed to vary from 0 at the interior limit of the damping layer to a maximum value on Γ_∞ according to a power law,

$$\sigma(\mathbf{x}) = \sigma_M \sum_i \left(\frac{x_i - x_i^{int}}{x_i^{ext} - x_i^{int}} \right)^\beta \tag{23}$$

where x_i^{int} and x_i^{ext} the coordinates of the interior and exterior limits of the absorbing layer, limits that lie along planes on which one coordinate is constant.

On the source surface Γ_f, a linear combination of incoming spinning modes can be specified. For a single spinning mode with azimuthal order s and radial order d, usually denoted as (s, d), the perturbation of the flow variables from the mean flow quantities (denoted by bars) is given by [22, 16]:

$$\begin{pmatrix} p - \bar{p} \\ \rho - \bar{\rho} \\ v_x - \bar{v}_x \\ v_r - \bar{v}_r \\ v_\theta - \bar{v}_\theta \end{pmatrix} = A \begin{pmatrix} E_m(k_{md} r) \cos\Theta \\ \frac{1}{\bar{c}^2} \cdot E_m(k_{md} r) \cos\Theta \\ \frac{k_x}{\omega_r \bar{\rho}} \cdot E_m(k_{md} r) \cos\Theta \\ \frac{k_{xd}}{\omega_r \bar{\rho}} \cdot E'_m(k_{md} r) \sin\Theta \\ \frac{m}{r\omega_r} \cdot E_m(k_{sd} r) \cos\Theta \end{pmatrix}, \tag{24}$$

where $\Theta = k_x x + m\theta - \omega_r t$, $k_{md} = \sqrt{(\omega_r/c)^2 - {k_x}^2}$, and $\omega_r = \frac{\omega \cdot R}{c_\infty}$. The function $E_m(k_{md} r) = J_m(k_{md} r) + q Y_m(k_{md} r)$ is the duct eigenfunction with J_m and Y_m denoting the Bessel functions of the first and second kind, respectively. For this configuration, the source surface is the unit radius circular disc centered at $(34.7, 4.6, 5.3)$.

3. RESULTS AND DISCUSSION

3.1. Flight data

The flight data on the twin-engine business jet was acquired at flight Mach number $M_\infty = 0.3$ at an altitude of 500 feet. The average Mach number at the source disc based on the mass flux through the engine was approximately $M_f = 0.53$. The blade passing frequency (BPF) was measured using several Kulite microphones located on the suction side of the wing at different angles from the nacelle axis as shown in Fig. 3. Only one

experimental data set, collected at the maximum power setting of the engine, was made available. This data consisted in the sound pressure level (SPL) at different points on the wing, normalized such that the SPL value at 20 degrees was equal to zero.

3.2. Time domain results

In order to determine the effect of the mode order on the inlet tone noise, propagation and radiation of azimuthal spinning modes $(18, 0)$ and $(22, 0)$ was simulated individually in the time domain in an otherwise quiescent medium around the aircraft. The measured BPF tone corresponded to a reduced frequency $\omega_r = 26.3$. The Euler equations were solved by the discontinuous Galerkin spectral element method on an unstructured grid with $103,105$ elements. The solution was approximated by a sixth-order Legendre polynomial in each element, so that the total number of Gauss-Legendre discretization points was $22,270,680$ in the computational domain that included the damping layers. The grid was constructed such that in the coarse part of the domain (in the vicinity of the inner boundary of the damping layer) the resolution averaged more than 5 points per wavelength. The resolution varied smoothly to reach more than twice this value inside the nacelle, where the elements are smaller in size but the order of the approximating polynomial is the same. The computations occupied one node (32 processors running at 1.1GHz clock speed) of an IBM Regatta-type SP4 machine. Each run lasted about 10 days. An arbitrary value of 10^{-4} times the ambient pressure was used for the amplitude of the dominant incoming mode, since the actual flight value was not known from the experiments. Therefore, for the purpose of comparison, computational data was matched with the flight data at the 60 degrees microphone location, where the peak SPL was observed.

Fig. 4 shows a snapshot of the acoustic pressure contours for spinning mode $(18, 0)$ on the surface of the aircraft at non-dimensional time $t = 44$, immediately before starting integration for the RMS pressure computation, and Fig. 5 the corresponding SPL contours. The SPL results from the runs with the spinning modes $(22, 0)$ and $(18, 0)$ radiated at the reduced frequency 26.3 for a stationary aircraft are plotted for the various angular locations on the wing in Fig. 6 and Fig. 7, respectively. Next, a combination of modes as shown in Tab. 1 was considered as a source. The modal amplitudes are in agreement with the duct measurements on the isolated engine for 88 percent speed [21], with the assumption that most energy is in the first radial mode. The phase has been chosen arbitrarily. Computed SPL values

in this case are shown in Fig. 8. The presence of lower-order modes together with the dominant mode $(22, 0)$ seems to bring the computation closer to the experiment, while a large SPL value is still obtained for the position at 70 degrees.

Mode	Ampl.	Phase (deg.)
(22,0)	0.81	30
(21,0)	1.0	0
(20,0)	0.48	45
(19,0)	0.15	45

Table 1: Relative modal amplitude and phase for the four modes used to specify the source.

The above results seem to indicate that the SPL distribution associated with the radiation of lower-order circumferential modes, i.e. $(18, 0)$, is closer to the experimental data than that of mode $(22, 0)$. However, this result may be due to the mean flow effects. Indeed, increasing the mean flow Mach number in the duct from its zero value assumed for these preliminary results would determine the modes to be more cut-on. An immediate effect would be that the main radiation lobe of all modes will hit the wing at a lower angle location. Thus, SPL levels at angles lower than 60 degrees are expected to increase, while decreasing at 70 degrees. The mean-flow effect, on the other hand, is expected to be in the opposite sense, but not as strong. It must also be considered that other sources of noise, not modeled in this computation (e.g., airframe noise) are responsible for higher SPL values at larger distances from the engine (i.e., at lower angles in the figures).

3.3. Frequency domain results

The current frequency domain formulation accommodates an inviscid, incompressible, irrotational, steady mean flow. We employed this formulation to study the noise field of the twin-jet business aircraft in flight. Our computing resources were limited to 192 processors of the same IBM SP4 machine. Since sparse direct solvers were used for the interior problem matrices A^p_{II}, this limitation confined our largest computation to a mesh of $103,105$ quartic elements leading to a total of $6,746,736$ discretization points. This resulted in a complex matrix with a total of 1.4 billion non-zero elements, whose storage even in sparse mode necessitated approximately 20GB memory. This resolution did not allow us to handle the exact flight conditions

of flight Mach number $M_\infty = 0.3$ and fan face Mach number $M_f = 0.53$. Therefore, we considered a test case with the flight Mach number $M_\infty = 0.1$ and the fan face Mach number $M_f = 0.2$. For these conditions, the grid resolution varied between 6 points per wavelength near the nacelle (where a finer grid compensates for the smaller wavelength due to the mean flow) to slightly above 3 points per wavelength towards the outer boundary of the domain. Each run on 192 processors required 2.5 days to obtain more than three orders of magnitude convergence. This clearly demonstrates the need for a better multi-level preconditioner for the reduced matrix S. However, we note that, to our knowledge, this is the largest complex linear algebra problem of this type reported in the literature.

Results from this simulation for mode $(18, 0)$ are presented in Fig. 9, which shows that the presence of the mean flow has the anticipated effects as discussed above. Indeed, the $M = 0.2$ flow in the duct causes the $(18, 0)$ mode to become more "cut-on", thus increasing the SPL immediately in front of the nacelle. Due however to the $M_\infty = 0.1$ mean flow around the aircraft, the drop in SPL towards the leading edge of the wing is steeper.

4. CONCLUSIONS

Recent progress in computational methods and computer architecture make direct computation of sound propagation in the near field of an aircraft engine inlet feasible. Two computer models designed for this purpose have been presented in this paper. Both methods are implemented using message passing to allow the use of modern, distributed memory machines. The time domain model uses the full nonlinear inviscid equations and can thus account for possibly high levels of sound amplitude at the source. It also solves for the full range of frequencies up to the limit of resolution. It requires relatively low computer memory resources, but the simulations may last a longer time before the acoustic field is established. The complementary frequency domain linear method is able to produce the solution for one driving frequency faster if enough memory is available. While a better preconditioner is still needed for this method, we must point out that the solution of complex linear algebra problems associated with the discretization of Helmholtz-type equations is a well-known issue in the numerical analysis and parallel computing community, and no satisfactory solution has been found yet.

The two methods have been used to compute sound propagation out of a two-engine business jet fan inlet. Results compared with available near-field experimental data show that the correct variation on the wing can be

reproduced in the computations. Effort is currently underway to incorporate various types of mean flow (possibly provided by experiment or independent computations) and do a systematic study of the effects of mean flow and modal composition of the source on the established sound field.

5. ACKNOWLEDGEMENTS

The authors want to thank Don Weir and Todd Wolownik of Honeywell Engines and Systems for their help with the experimental data. The support of NASA through grant NAG-1-01031 is gratefully acknowledged.

References

[1] Balay, S., Gropp, W.D., McInnes, L.C. and Smith, B.F., "PETSc Users Manual," ANL-95/11 Revision 2.1.1, Argonne National Laboratory, 2001.

[2] Canuto, C., Hussaini, M.Y., Quarteroni, A. and Zang, T.A., *Spectral Methods in Fluid Dynamics*, Springer-Verlag, 1988.

[3] Gordon, W.J. and Hall, C.A., "Construction of curvilinear co-ordinate systems and applications to mesh generation," *International Journal for Numerical Methods in Engineering* Vol. 7, 1973, pp.461-477.

[4] Hirsch, C., *Numerical Computation of Internal and External Flows. Volume 2: Computational Methods for Inviscid and Viscous Flows*, John Wiley & Sons, 1990.

[5] Hu, F.Q., Hussaini, M.Y. and Rasetarinera, P., "An Analysis of the Discontinuous Galerkin Method for Wave Propagation Problems," *Journal of Computational Physics* Vol. 151, 1999, pp.921-946.

[6] Nallasamy, M., "Computation of Noise Radiation from Fan Inlet and Aft Ducts," *Journal of Aircraft*, Vol. 34, 1997, pp.387-393.

[7] Ozyoruk, Y. and Long, L.N., "Computation of Sound Radiating from Engine Inlets," *AIAA Journal*, Vol. 34, 1996, pp.894-901.

[8] Parrett, A.V., and Eversman, W., "Wave Envelope and Finite Element Approximations for Turbofan Noise Radiation in Flight," *AIAA Journal*, Vol. 24, 1986, pp.753-760.

[9] Patera, A. T., "A Spectral Element Method for Fluid Dynamics: Laminar Flow in a Channel Expansion," *Journal of Computational Physics* Vol. 54, 1984, pp.468-488.

[10] Rasetarinera, P., Hussaini, M.Y. and Hu, F.Q., in *Discontinuous Galerkin Methods*, Lecture Notes in Computational Science and Engineering **11** 407-412, B. Cockburn, G.E. Karniadakis and C.-W. Shu, Editors, Springer-Verlag, Berlin, 2000.

[11] Rasetarinera, P., Kopriva, D.A., and Hussaini, M.Y., "Discontinuous Spectral Element Solutions of Acoustic Radiation from Thin Airfoils," *AIAA Journal* Vol. 39, 2001, pp.2070-2075.

[12] Rasetarinera, P. and Hussaini, M.Y., "An Efficient Implicit Discontinuous Spectral Galerkin Method," *Journal of Computational Physics* Vol. 172, 2001, pp.718-738.

[13] Rebay, S., "Efficient Unstructured Mesh Generation by Means of Delaunay Triangulation and Bowyer-Watson Algorithm," *Journal of Computational Physics* Vol. 106, 1993, pp.125-138.

[14] Roe, P.L., "Approximate Riemann Solvers, Parameter Vectors, and Difference Schemes," *Journal of Computational Physics* Vol. 43, 1981, pp.357-372.

[15] Stanescu, D. and Habashi, W.G., "2N-Storage Low Dissipation and Dispersion Runge-Kutta Schemes for Computational Acoustics," *Journal of Computational Physics* Vol. 143, 1998, pp.674-681.

[16] Stanescu, D., Ait-Ali-Yahia, D., Habashi, W. G., and Robichaud, M.P., "Multidomain Spectral Computations of Sound Radiation from Ducted Fans," *AIAA Journal* Vol. 37, 1999, pp.296-302.

[17] Stanescu, D., Ait-Ali-Yahia, D., Habashi, W. G., and Robichaud, M.P., "Galerkin Spectral Element Method for Fan Tone Radiation Computations," AIAA Paper 2000-1912, 6th AIAA/CEAS Aeroacoustics Conference, Lahaina, Hawaii.

[18] Stanescu, D., Kopriva, D.A. and Hussaini, M.Y., "Dispersion Analysis for Discontinuous Spectral Element Methods," *Journal of Scientific Computing* Vol. 15, 2000, pp.149-171.

[19] Stanescu, D., Hussaini, M.Y. and Farassat, F., "Aircraft Engine Noise Scattering - A Discontinuous Spectral Element Approach," AIAA Paper 2002-0800, Reno, NV.

[20] Stanescu, D., Hussaini, M.Y. and Farassat, F., "Large Scale Frequency Domain Numerical Simulation of Aircraft Engine Tone Noise Radiation and Scattering," AIAA Paper 2002-2586, 8th AIAA/CEAS Aeroacoustics Conference, Breckenridge, CO.

[21] Sutliff, D.L., Konno, K.E., and Heidelberg, L.J., "Duct Mode Measurements on the TFE731-60 Full Scale Engine," AIAA Paper 2002-2564, 8th AIAA/CEAS Aeroacoustics Conference, Breckenridge, CO.

[22] Tyler, J. M. and Sofrin, T. G., "Axial Flow Compressor Noise Studies," *SAE Transactions* Vol. 70, 1962, pp.308-332.

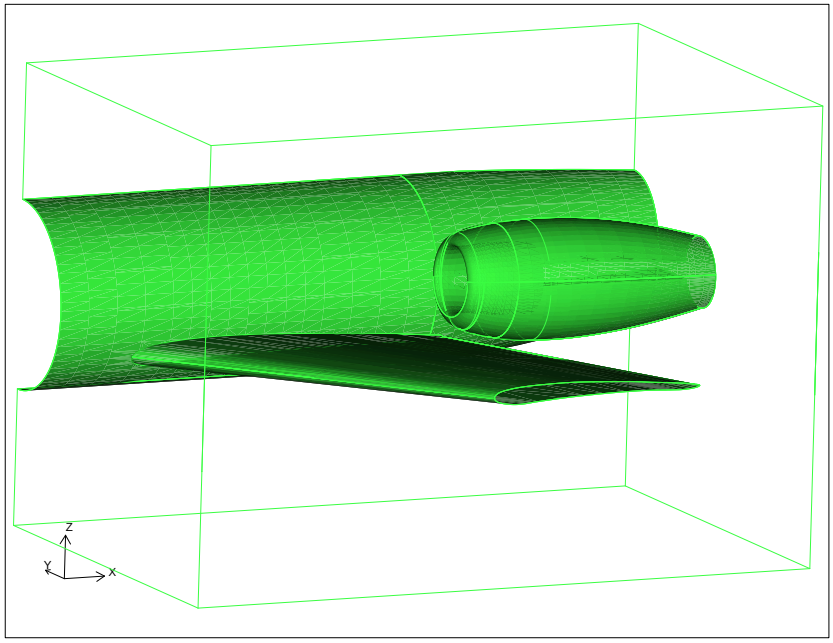

Figure 1: Computational domain.

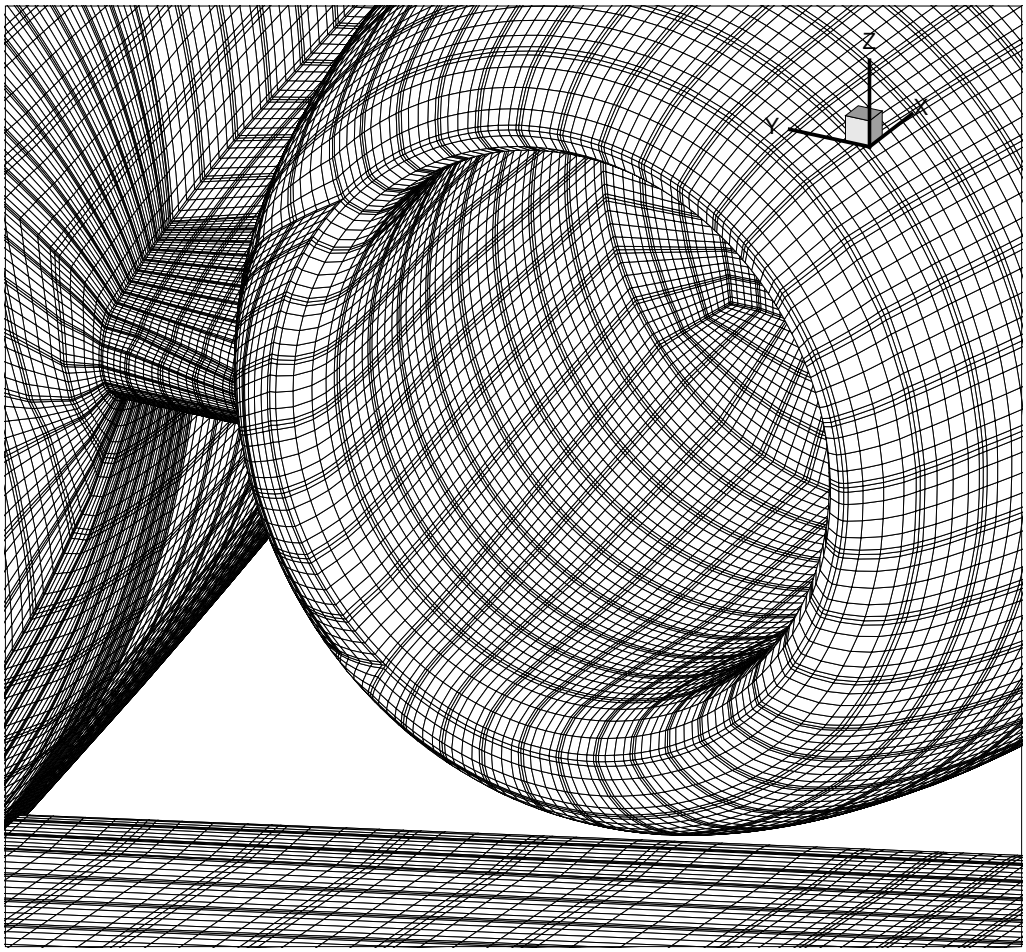

Figure 2: Mesh on the aircraft surface for $N = 6$ (sixth order elements).

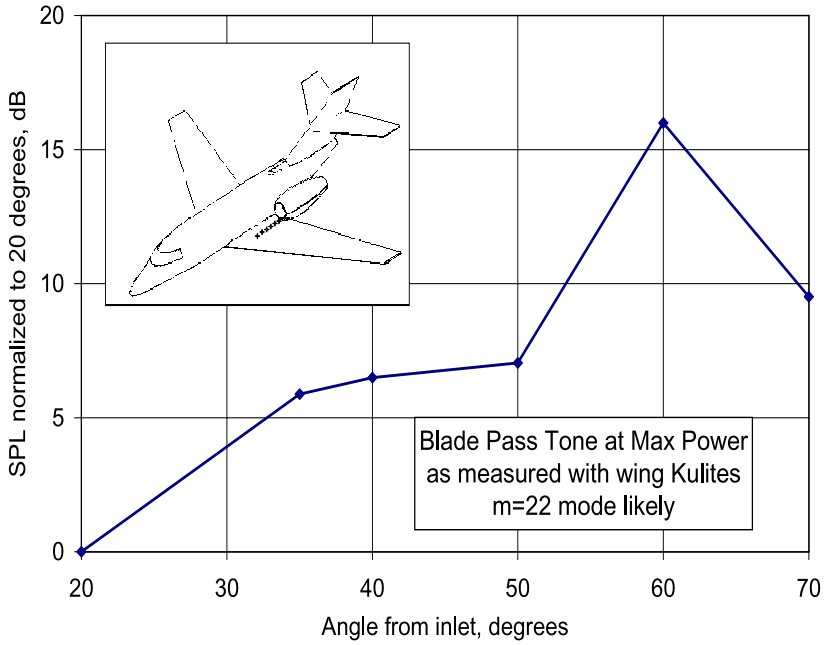

Figure 3: Location of microphones on the wing and corresponding experimental data.

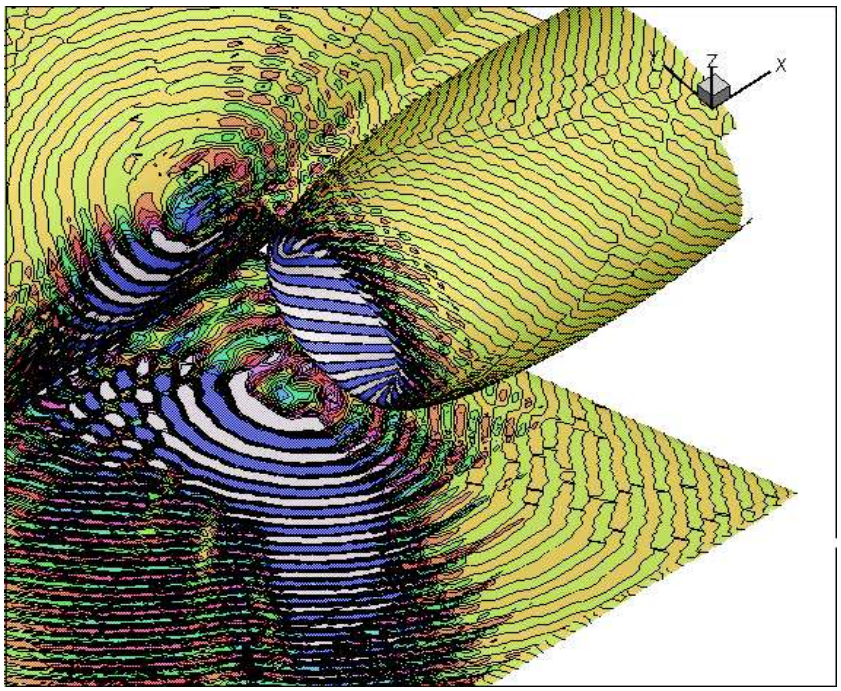

Figure 4: Acoustic pressure contours on the aircraft surface. Mode (18,0) radiated at $\omega_r = 26.3$.

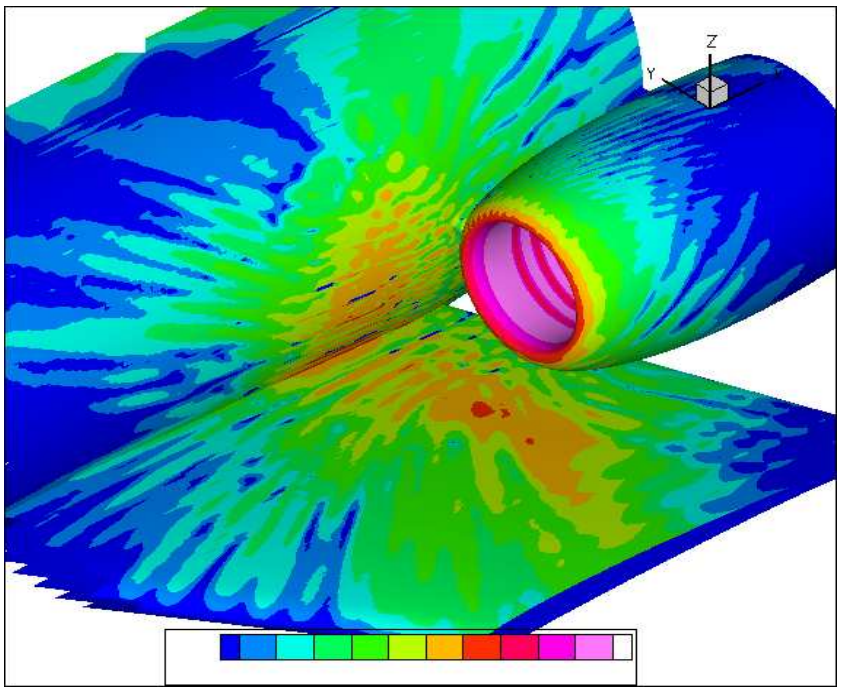

Figure 5: SPL contours on the aircraft surface. Mode (18,0) radiated at $\omega_r = 26.3$.

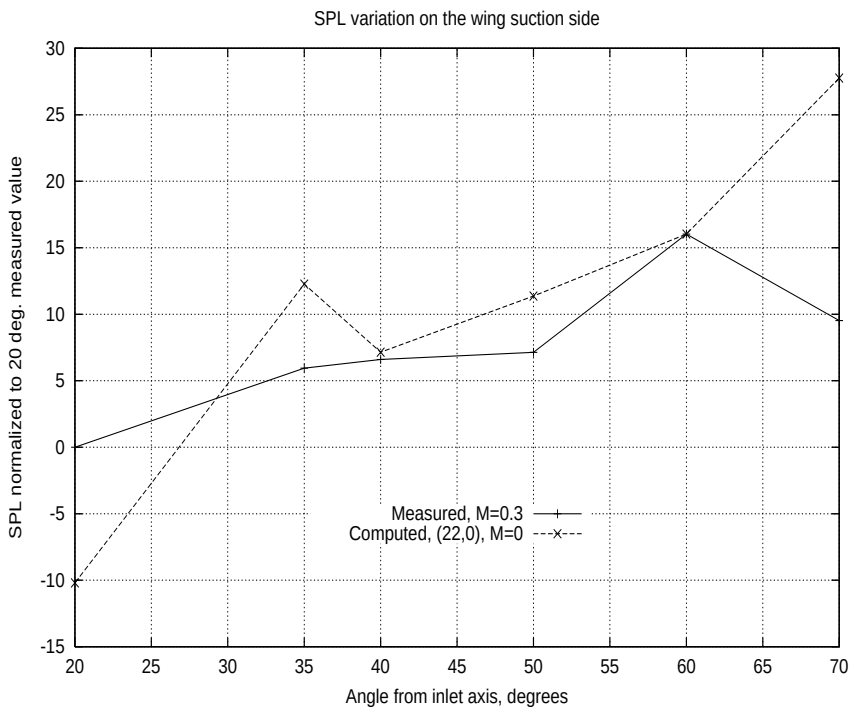

Figure 6: SPL levels on the wing surface for mode (22,0) radiated at $\omega_r = 26.3$ in a quiescent medium.

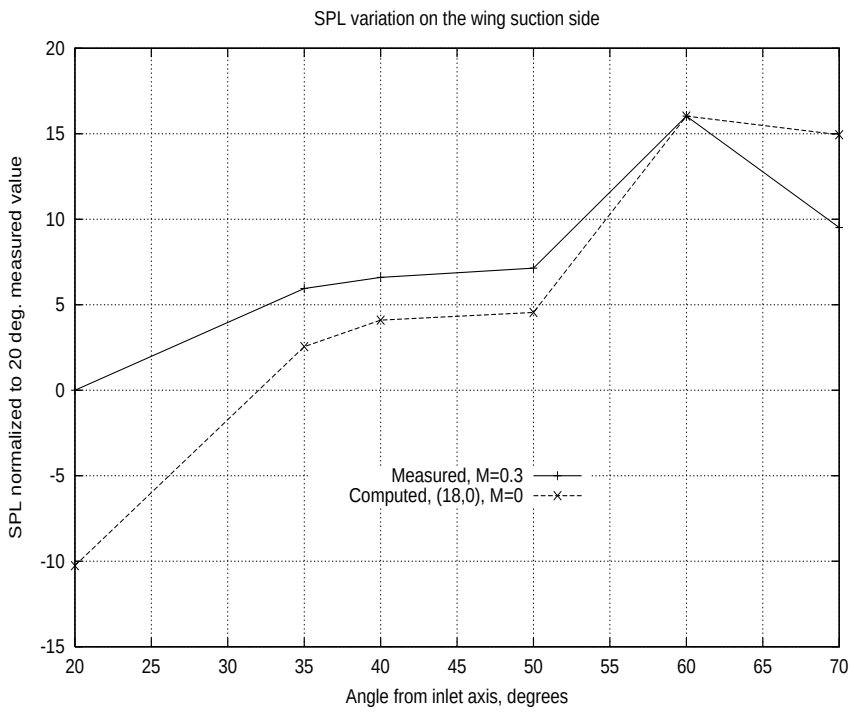

Figure 7: SPL levels on the wing surface for mode (18,0) radiated at $\omega_r = 26.3$ in a quiescent medium.

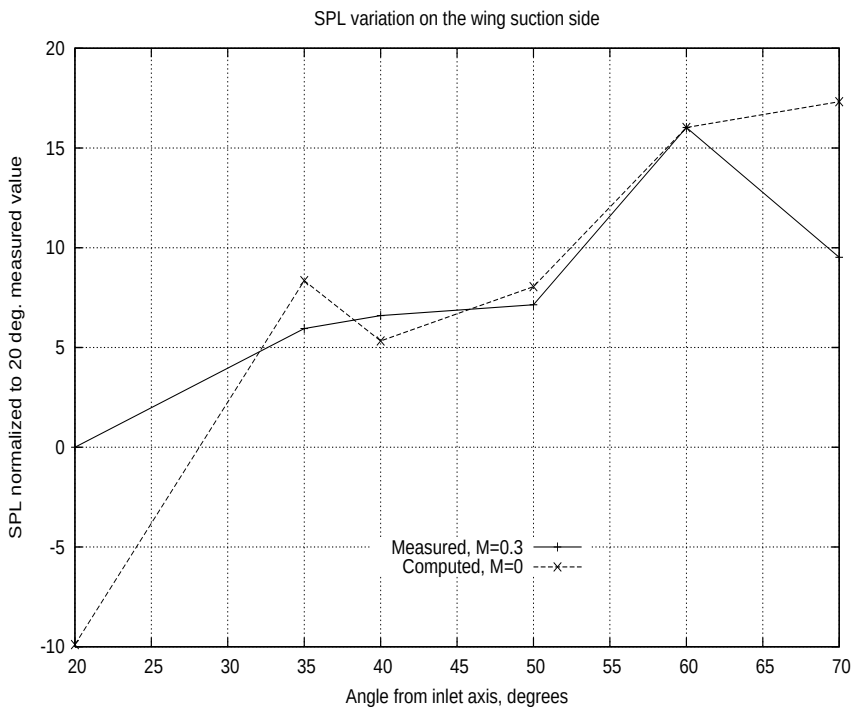

Figure 8: SPL levels on the wing surface for the four modes source at $\omega_r = 26.3$ in a quiescent medium.

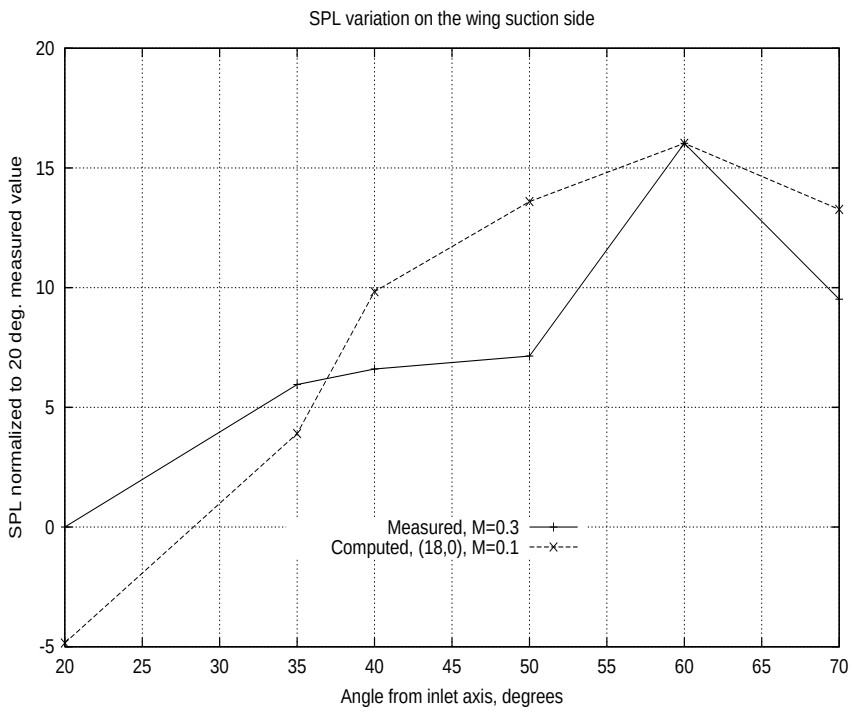

Figure 9: SPL levels on the wing surface for mode (18,0) radiated at $\omega_r = 26.3$ in the presence of mean flow.